

Article

Mass and Heat Transfer Coefficients in Automotive Exhaust Catalytic Converter Channels

Chrysovalantis C. Templis and Nikos G. Papayannakos *

School of Chemical Engineering, National Technical University of Athens, 9, Heroon Polytechniou Str., Gr-15780 Zografos, Athens, Greece; valantis2010@yahoo.gr

* Correspondence: npap@central.ntua.gr; Tel.: +30-210-772-3239; Fax: +30-210-772-3155

Received: 9 May 2019; Accepted: 3 June 2019; Published: 4 June 2019



Abstract: Mass and heat transfer coefficients (MTC and HTC) in automotive exhaust catalytic monolith channels are estimated and correlated for a wide range of gas velocities and prevailing conditions of small up to real size converters. The coefficient estimation is based on a two dimensional computational fluid dynamic (2-D CFD) model developed in Comsol Multiphysics, taking into account catalytic rates of a real catalytic converter. The effect of channel size and reaction rates on mass and heat transfer coefficients and the applicability of the proposed correlations at different conditions are discussed. The correlations proposed predict very satisfactorily the mass and heat transfer coefficients calculated from the 2-D CFD model along the channel length. The use of a one dimensional (1-D) simplified model that couples a plug flow reactor (PFR) with mass transport and heat transport effects using the mass and heat transfer correlations of this study is proved to be appropriate for the simulation of the monolith channel operation.

Keywords: Mass transfer coefficients; heat transfer coefficient; automotive converter; CFD calculations

1. Introduction

The growing concern about the environmental impact of the exhaust emission pollutants has led to the need for the development of increasingly efficient exhaust gas after-treatment systems and catalytic converters [1].

In gasoline engine applications, the toxicity of exhaust emissions is reduced by employing catalytic converters as an afterburning reactor [2]. The catalytic converter is usually a multiple-channel reactor with a honeycomb structure. The catalytic combustion reactions occur in a thin washcoat of a catalyst on the reactor wall [3]. Although the flow in the exhaust piping of an engine is normally turbulent, Reynolds (Re) numbers in the converter monolith channels are always safely in the laminar region ($Re < 300$) [4] with fully developed flow in the greatest part of the reactor [3]. These structured reactors are characterized by enhanced heat and mass transfer, relatively low pressure drop, large geometric surface area and high catalyst efficiency due to the low thickness of the catalyst film that is deposited on the substrate wall and in which the heterogeneous chemical reactions take place [5].

A major simplification in models used in the literature is to represent the multiple-channel reactor by a single channel with the assumption of equivalent passages with no interaction [6,7]. The catalyst is assumed to be perfectly insulated and it is exposed to a uniform flow. The effects of thermal gradients in the radial direction are considered to be insignificant and the temperature and concentration profiles are assumed to be the same in all channels [6]. These assumptions simplify the problem significantly leading to a “single channel” model, and the performance predicted for one channel can be extended to the entire reactor [1].

Two broadly classified hierarchical models are used in the literature: Three- or two-dimensional (3-D or 2-D) convection–diffusion models with a wall reaction [8–11] and 1-D models, which describe

the axial variation of a radially average concentration and temperature in a channel cross-section [2,6,8,12–14]. Over the years, 1-D models became more popular because of their simplicity and the less computational time required for the solution of the pertinent differential equations [6] while they provide sufficiently accurate predictions and also allow for fast kinetic investigations.

The catalyst performance is influenced by the mass and heat transfer from the exhaust gases to the catalyst surface [2]. Hence, a correct description of the mass and heat transfer processes is important in catalyst models and simulation. The mass and heat transfer coefficients introduced in the 1-D models are often expressed in terms of dimensionless numbers Sherwood (Sh) and Nusselt (Nu) and they depend on various parameters, such as shape and dimensions of the channel, fluid properties, flow rates, washcoat characteristics and reaction rates [7,15]. It is very difficult, if not impossible, to experimentally measure local concentrations and temperatures, and especially wall concentrations and temperatures in narrow channel monoliths [16], but the mass and heat transfer coefficients may be computed from the radial temperature and concentration gradients computed by using two or three dimensional models [3,7].

Various correlations have been proposed concerning the mass transfer coefficient in monolithic reactors based on experiments [6,8,17–21]. Correlations of heat and mass transfer coefficient based on numerical solutions through channels have also been published in literature [12,15,17,22–26]. The experimentally estimated values of transfer coefficients correspond to the average values in the reactor, while estimations from numerical solutions resulted in coefficients as a function of channel length.

For the mass/heat transport two limiting cases of boundary conditions are extensively discussed in the literature for common channel geometries. In the one case the concentration/temperature on the wall is considered constant (Nu_T , Sh_T) and in the other one the mass and heat fluxes to and through the wall is constant (Nu_F , Sh_F). However, in the case of catalytically reacting fluids the boundary conditions at the wall are not constant, which might lead to different values of Nu and Sh numbers. Groppi et al. [27] proposed an interpolation formula between Nu_T and Nu_F with the introduction of the Damkohler number (Da) for the calculation of the local Nu at reacting conditions.

Using a constant value for Sherwood and Nusselt numbers and not taking into account the dependence on the velocity or position and reaction parameters may lead to the incorrect prediction of the ignition and extinction points for exothermic surface catalyzed reactions [2,15]. Since Sherwood and Nusselt numbers can have a significant effect on the predicted emissions for automotive catalysts, accurate knowledge of mass transfer coefficients is essential for 1-D mathematical modeling of the converter performance [6] and local values of heat and mass transfer coefficients are needed for the correct simulation of the monolithic converters operation [2,3].

Sh correlations in monolith channels at reaction conditions have been proposed in the literature [15], however they have been derived considering only one first order reaction taking place in the washcoat. Arrighetti et al. [11] used a computational fluid dynamics three-dimensional (3-D) model coupled to a surface chemistry solver (Cantera) for the calculation of Sh and Nu along the monolith length in a multi-component gas phase, but they did not propose any correlation. The latter publication indicates that the traditional correlations, as well as the use of heat/mass transfer analogy that is commonly used in simulations, may give remarkable errors in the evaluation of the converter performance. Hayes and Kolaczkowski [16], Groppi et al. [27] and Heck et al. [28] calculated Nu at non-isothermal reacting conditions but they did not provide correlations of the Sh and Nu with the operating conditions and the position of the channel.

The objective of this work is the estimation and the development of correlations for mass transfer coefficients of species and heat transfer coefficient from the bulk of the gas phase to channel wall according to the thin film theory, considering a real multi-component gas mixture and representative kinetics of the reactions taking place on the channel wall of automotive converters. The MTCs and HTC were calculated and correlated for a circular channel as most of the monolith cross section shapes, square, hexagonal and of course circular, closely resemble a circular cross section after wash coating

during which the wash coat preferentially covers the edges of the monolithic structures. The transfer coefficients were correlated along the monolith cell length using dimensionless numbers taking into account fluid properties and geometric characteristics. The proposed correlations have been developed for a wide range of velocities and conditions and therefore, they can be used in simulation studies not only from lab up to real size automotive catalytic converters but also for a wide range of monolithic reactors operating with gas feeds.

2. Models

2.1. 2-D Computational Fluid Dynamic (CFD) Models

The mass transfer coefficients of each species in the gas mixture and the heat transfer coefficient were calculated along the monolith channel length according to the thin film theory by developing and running detailed 2-D computational fluid dynamic (CFD) models in Comsol Multiphysics and combining their results with a 1-D model in which mass and heat transfer coefficients account for transport phenomena. For the determination of the mass transfer coefficients, an isothermal CFD model incorporating the momentum and mass transport phenomena inside the monolith channel was used. For the determination of the heat transfer coefficient, a non-isothermal CFD model incorporating in detail the momentum, mass and heat transport in the monolith channel was employed.

The CFD calculations were performed by considering a typical monolithic converter with cylindrical cells of 1.1 mm internal diameter and a 2-D geometry of the cylindrical monolith channel with axial symmetry.

The computation of heat and mass transfer fluxes requires the knowledge of kinetics, and the kinetic model is of crucial importance in the calculation of the total conversion rates and evidently of the pertinent transfer coefficients. In this study, a technical kinetic model of the reactions taking place in a typical commercial automotive converter was used. All the reactions were considered to be heterogeneously catalyzed by the active species in the washcoat on the channel walls. The technical kinetic model was determined using experimental data that were obtained with a commercial cordierite monolithic converter in crushed form and a size range of 250–350 μm . All the data for the estimation of the reaction kinetics are given in Supplementary Materials (S.M.).

2.1.1. Isothermal 2-D CFD Model

The isothermal CFD model incorporates in detail the momentum and mass transport through the monolith channel at isothermal conditions.

For the momentum transport the Incompressible Navier Stokes equations were used to describe the laminar and isothermal flow of the gas mixture.

$$\rho \mathbf{u} \cdot \nabla \mathbf{u} = \nabla \cdot \left[-p \mathbf{I} + \mu (\nabla \mathbf{u} + (\nabla \mathbf{u})^T) \right], \quad (1)$$

$$\nabla \cdot \mathbf{u} = 0. \quad (2)$$

The gas phase was considered to be a mixture of ideal gases. The no slip condition was set on the channel wall. Normal inflow velocity was set as the boundary condition at the inlet of the channel and the ambient pressure and no viscous stress condition was set at the cell outlet.

A convective and diffusive model according to Fick's law was used to describe mass transport in the gas phase as the diffusing species were dilute with respect to the abundant N_2 .

$$\nabla \cdot (-D_i \nabla C_i) + \mathbf{u} \cdot \nabla C_i = 0. \quad (3)$$

The heterogeneous reactions that take place on the washcoat were set as a mass flux boundary condition on the wall of the washcoat that is in contact with the gas phase. No diffusion in the normal direction was considered at the outlet (convective flux boundary condition). The gas feed composition

was set as the boundary condition at the cell inlet. Convective transport inside the porous washcoat was neglected.

The boundary conditions for the momentum and mass transport in the isothermal CFD model are summarized in Table 1.

Table 1. Boundary conditions for the momentum and mass transport in the isothermal 2-D computational fluid dynamic (CFD) model for the determination of the gas–solid mass transfer coefficients.

Boundary	Momentum Transport	Mass transport
Symmetry boundary	Axial Symmetry $r = 0$	Axial Symmetry $r = 0$
Substrate wall	No Slip $\mathbf{I} \cdot \mathbf{u} = 0$	Mass Flux (Reaction Rate R_i) $-\mathbf{n} \cdot (-D_i \nabla C_i + C_i \cdot \mathbf{u}) = R_i$
Inlet	Normal Inflow Velocity: $\mathbf{u} = -u_{in} \mathbf{n}$	Feed Composition $C_i = C_{i,in}$
Outlet	Ambient Pressure, No Viscous Stress $p = 101323 \text{ Pa}$ $\mu(\nabla \mathbf{u} + (\nabla \mathbf{u})^T) \mathbf{n} = 0$	Convective Flux (No Diffusion in the Normal Direction) $\mathbf{n}(-D_i \nabla C_i) = 0$

2.1.2. Non-Isothermal 2-D CFD Model

The non-isothermal CFD model incorporates in detail the momentum, mass and heat transport through the monolith channel. For the CFD calculations, momentum, mass and heat transport partial differential equations (PDE's) were coupled and solved simultaneously.

For the momentum transport the weakly compressible Navier Stokes equations were used to describe the laminar and non-isothermal flow of the gas mixture through the channel,

$$\rho \mathbf{u} \cdot \nabla \mathbf{u} = \nabla \cdot \left[-p \mathbf{I} + \mu(\nabla \mathbf{u} + (\nabla \mathbf{u})^T) - \frac{2\mu}{3}(\nabla \cdot \mathbf{u}) \mathbf{I} \right], \quad (4)$$

$$\nabla \cdot (\rho \mathbf{u}) = 0. \quad (5)$$

A convective and diffusive model according to Fick's law was also used in this model to describe mass transport in the gas phase as the diffusing species were dilute with respect to N_2 excess,

$$\nabla \cdot (-D_i \nabla C_i + C_i \mathbf{u}) = 0. \quad (6)$$

For the heat transport, a convective and conductive model was used to describe the heat transport in the gas phase,

$$\nabla \cdot (-k \nabla T) = -\rho C_p \mathbf{u} \nabla T, \quad (7)$$

$$\rho = M_n \frac{(P + P_{ref})}{R_g T}. \quad (8)$$

In the gas phase, there was no heat source or sink, as the homogeneous reactions were not taken into account. As the reaction was considered taking place on the wall of the washcoat, which is in contact with the gas phase, similarly the heat of reaction released was set as a boundary condition on the wall,

$$q(T) = \sum -R_j \cdot \Delta HR_j(T). \quad (9)$$

The channel was considered to be adiabatic. No conduction in the normal direction was considered at the gas phase outlet (convective flux boundary condition). The inlet gas feed temperature was set as the boundary condition at the cell inlet.

The boundary conditions for the momentum, mass and heat transport in the non-isothermal 2-D CFD model are summarized in Table 2.

Table 2. Boundary conditions for the momentum, mass and heat transport in the non isothermal 2-D CFD model.

Boundary	Momentum Transport	Mass transport	Heat transport
Symmetry boundary	Axial Symmetry $r = 0$	Axial Symmetry $r = 0$	Axial Symmetry $r = 0$
Substrate wall	No Slip II. $\mathbf{u} = 0$	Mass Flux (Reaction Rate R_i) $-\mathbf{n} \cdot (-D_i \nabla C_i + C_i \cdot \mathbf{u}) = R_i$	Heat flux $-\mathbf{n} \cdot (-k \nabla T + \rho C_p T \mathbf{u}) = \sum_j -R_j \cdot \Delta H R_j$
Inlet	Normal Inflow Velocity: $\mathbf{u} = -u_{in} \mathbf{n}$	Feed Composition $C_i = C_{i,in}$	Feed Temperature $T = T_{in}$
Outlet	Ambient Pressure, No Viscous Stress $p = 101323 \text{ Pa}$ $[\mu(\nabla \mathbf{u} + (\nabla \mathbf{u})^T) - \frac{2\mu}{3}(\nabla \cdot \mathbf{u})\mathbf{I}]\mathbf{n} = 0$	Convective Flux (No Diffusion in the Normal Direction) $\mathbf{n} \cdot (-D_i \nabla C_i) = 0$	Convective Flux (No Conduction in the Normal Direction) $\mathbf{n} \cdot (-k \nabla T) = 0$

2.2. 1-D Thin Film Model

A 1-D simplified model that couples a plug flow reactor (PFR) with mass and heat transport effects according to the thin film theory, using the correlation for mass and heat transfer of this study, has been developed. The mathematical model consists of the differential mass balances, one for each component that takes part in the reactions and appears in the kinetic model, the differential heat balance and the algebraic equations for mass and heat transfer.

$$\frac{dC_{CO,b}}{dz} = \frac{(-R_1 - R_5 + 3 \cdot R_6 + R_7 + 3 \cdot R_8) \cdot S_v}{u}, \quad (10)$$

$$\frac{dC_{NO,b}}{dz} = \frac{-R_5 \cdot S_v}{u}, \quad (11)$$

$$\frac{dC_{CH_4,b}}{dz} = \frac{(-R_2 - R_7) \cdot S_v}{u}, \quad (12)$$

$$\frac{dC_{C_3H_6,b}}{dz} = \frac{(-R_3 - R_8) \cdot S_v}{u}, \quad (13)$$

$$\frac{dC_{C_3H_8,b}}{dz} = \frac{(-R_4 - R_6) \cdot S_v}{u}, \quad (14)$$

$$\frac{dC_{O_2,b}}{dz} = \frac{(-0.5 \cdot R_1 - 2 \cdot R_2 - 4.5 \cdot R_3 - 5 \cdot R_4) \cdot S_v}{u}, \quad (15)$$

$$\frac{dC_{H_2O,b}}{dz} = \frac{(2 \cdot R_2 + 3 \cdot R_3 + 4 \cdot R_4 - 3 \cdot R_6 - R_7 - 3 \cdot R_8) \cdot S_v}{u}. \quad (16)$$

At non-isothermal conditions, the differential heat balance is also solved.

$$\frac{dT_b}{dz} = \frac{\sum (-R_j \Delta H R_j) \cdot S_v}{\rho u C_p}. \quad (17)$$

The algebraic equations for mass transport of each component i according to the thin film theory is:

$$R_i = K_{gs,i}(C_{i,s} - C_{i,b}). \quad (18)$$

The algebraic equations for heat transport according to the thin film theory is:

$$\sum (-R_j \Delta H R_j) = K_t(T_s - T_b). \quad (19)$$

The reactions and the reaction rate equations are given by Equations S1.1–S8.2 involved in Supplementary Materials.

The differential mass balances were solved using the Runge Kutta 4th order method and Fortran programming language.

2.3. Conditions of Calculations

The calculations of the mass and heat transfer coefficients were performed for inlet temperatures 200, 300, 400 and 500 °C. Forty in total interstitial velocities (ten velocities at each temperature) within the range of 0.028–7.2 m/s covering the total range of the working conditions with a laboratory and real size monolith and two gas feed compositions, lean and rich as described in Table S1 given in Supplementary Materials, were tested. The gas–solid mass transfer coefficients for six species NO, CO, O₂, CH₄, C₃H₆ and C₃H₈ were calculated. A total cell length of 1 cm was tested for the low velocities and of 12 cm for the high velocities. The conditions selected to perform simulations for the calculation of the gas–solid mass transfer coefficients are summarized in Table 3.

Table 3. Simulation conditions for the determination of mass and heat transfer coefficients.

Inlet Temperatures (°C)	200, 300, 400 and 500
Velocities u_{in} (m/s)	0.028–7.2
Inlet Compositions	Rich, Lean
Cell length (cm)	1–12

At the tested conditions the flow of the gas phase through the monolith channel is laminar.

3. Mass Transfer Coefficients

3.1. Calculation of Effective Gas–Solid Mass Transfer Coefficient Profiles Along the Channel

The effective mass transfer coefficients $K_{gs,i}$ for each component i , were calculated according to the thin film theory, running the detailed 2-D CFD model and combining its results with the following 1-D model equation along the channel length:

$$(R_i)_z = (K_{gs,i})_z ((C_{i,s})_z - (C_{i,b})_z), \quad (20)$$

where $(R_i)_z$ represents the reaction rate at the position z of the cell length coordinate expressed per square meter of the washcoat wall, $(C_{i,s})_z$ corresponds to the component's i concentration at the position z of the cell length coordinate on the wash coat and $(C_{i,b})_z$ stands for the mean bulk concentration at the position z of the cell length coordinate. The mean concentration of the component i along the channel radius was calculated by Equation (21).

$$(C_{i,b})_z = \frac{(C_i \cdot \bar{u})_z}{(\bar{u})_z}, \quad (21)$$

where

$$(C_i \bar{u})_z = \left(\frac{1}{\pi R^2} \right) \int_{r=0}^{r=R} (C_i)_{z,r} \cdot (u)_{z,r} \cdot 2 \cdot \pi \cdot r \cdot dr, \quad (22)$$

$$(\bar{u})_z = \left(\frac{1}{\pi R^2} \right) \int_{r=0}^{r=R} (u)_{z,r} \cdot 2 \cdot \pi \cdot r \cdot dr. \quad (23)$$

The mass transfer coefficients change with the coordinate of the length, z . A typical profile of mass transfer coefficient along the monolith cell length is presented in Figure 1.

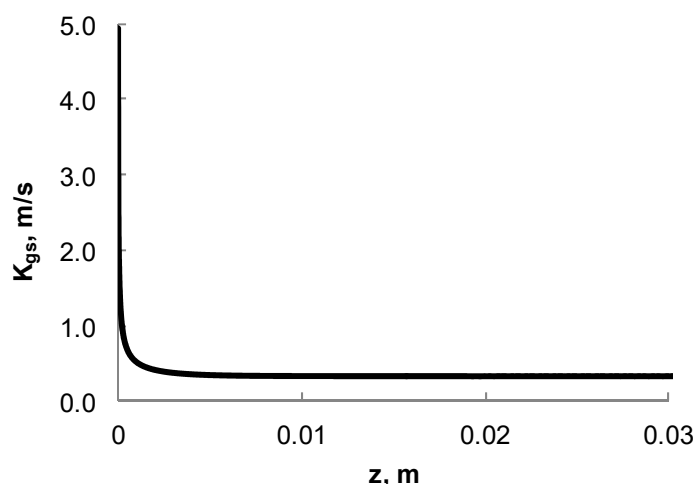


Figure 1. Typical profile of mass transfer coefficient along the monolith cell length.

As shown in Figure 1 the mass transfer coefficient near the entrance had a high value and it steeply decreased with length at the first millimeter from the cell entrance, and then after some millimeters it reached a plateau, and remained constant for the rest of the length. This is due to the fact that at the entrance of the channel the concentration of the reactants is uniform along the channel radius and the difference between the concentration in the bulk of the gas phase and in the gas phase over the washcoat is very small while the reaction rates are high due to the high surface concentration of the reactants. Thus, the mass transfer coefficient appears to be high close to the entrance and decreases with the channel length, as concentration profiles are developed along the radius.

3.2. Correlation of the Effective Gas–Solid Mass Transfer $K_{gs,i}$

The mass transfer coefficients were correlated along the monolith cell length using the dimensionless numbers of Sherwood, Schmidt and Reynolds numbers according to the following equation form, which has been proposed by Grigul and Tratz [22]:

$$\text{Sh}(z) = a + b \cdot (z^* \cdot 10^3)^c \exp(e \cdot z^*), \quad (24)$$

where:

$$z^* = \frac{z}{d} \frac{1}{\text{Re} \cdot \text{Sc}}, \quad (25)$$

$$\text{Sc} = \frac{\mu}{\rho D_i}, \quad (26)$$

$$\text{Re} = \frac{\rho u d}{\mu}, \quad (27)$$

$$\text{Sh} = \frac{K_{gs,i} \cdot d}{D_i}. \quad (28)$$

The parameter a is related to the $K_{gs,i}$ value at which the $K_{gs,i}$ profile is stabilized and reaches a plateau, the parameter b is related to the initial value that the $K_{gs,i}$ takes on the cell entrance and the parameters c and d are related to the curvature of the profile during the profile drop and the length from the entrance that is demanded for the $K_{gs,i}$ profile to be stabilized reaching a plateau.

The final correlation was derived using four hundred and eighty (480) profiles of gas–solid mass transfer coefficients $K_{gs,i}$ along the cell length at the tested conditions (six species, four temperatures for each species, 10 velocities at each temperature and two gas feed compositions). The Re number at the tested conditions lies within the range 0.51–122 and the Schmidt (Sc) number lies within the range 0.63–1.31.

3.2.1. Correlation Parameters

For the lean and the rich feed compositions the same correlation of the gas–solid mass transfer coefficient $K_{gs,i}$ resulted. For the best fitting of the correlation to the $K_{gs,i}$ profiles derived from CFD calculations and thus for their better prediction, different Sh correlations are proposed for the groups of species CO, NO and O₂ from one side and hydrocarbons CH₄, C₃H₆ and C₃H₈ to the other side. Sh correlations, which are chemical species dependent, have been also reported by Santos and Costa [6]. For an Re lower than 27.5, Re does not affect the $K_{gs,i}$ profile and in this case Re must be considered equal to 27.5 for all species for a better prediction of the proposed correlation.

Mass Transfer Correlation for Species CO, NO and O₂

For the species CO, NO and O₂ a branched correlation derived. The best fitting of the correlation to the $K_{gs,i}$ profiles derived from CFD calculations was achieved for parameters:

$$\left. \begin{array}{l} \text{if } u \frac{298}{T(K)} > 0.232 \text{ m/s} \\ \text{if } u \frac{298}{T(K)} < 0.232 \text{ m/s} \\ \text{while if } Re < 27.5 \end{array} \right\} \begin{array}{l} \Rightarrow a = 4.2, b = 18, c = -0.55, e = -40; \\ \Rightarrow a = 4.2 - 0.389 * \ln[u * 298 / T] - 0.5857, b = 18, c = -0.55, e = -70; \\ \Rightarrow Re = 27.5. \end{array}$$

Mass Transfer Correlation for Hydrocarbons CH₄, C₃H₆ and C₃H₈

For hydrocarbons also a branched correlation was derived. Using common correlation parameters for all the hydrocarbon species, the best fitting of the correlation to the $K_{gs,i}$ profiles derived from CFD calculations was achieved for the parameters reported below.

$$\begin{array}{ll} \text{For } Re > 0.51 & \Rightarrow a = 4.25, b = 16.5, c = -0.7, e = -40; \\ \text{while if } Re < 27.5 & \Rightarrow Re = 27.5. \end{array}$$

3.2.2. Mass Transfer Correlation Fitting

In Figure 2 typical cases of the correlation fitting to mass transfer coefficients $K_{gs,i}$ profile along the monolith cell as derived from CFD calculations are presented for all the species at the middle interstitial velocity and Re. In these Figures the concentration profiles of species in the bulk of the gas phase and in the gas phase over the catalytic surface are also presented. In Figure 2 the fitting up to length L/10 (where L is the total length of the monolith converter) is presented, while for the rest of the channel a plateau was reached.

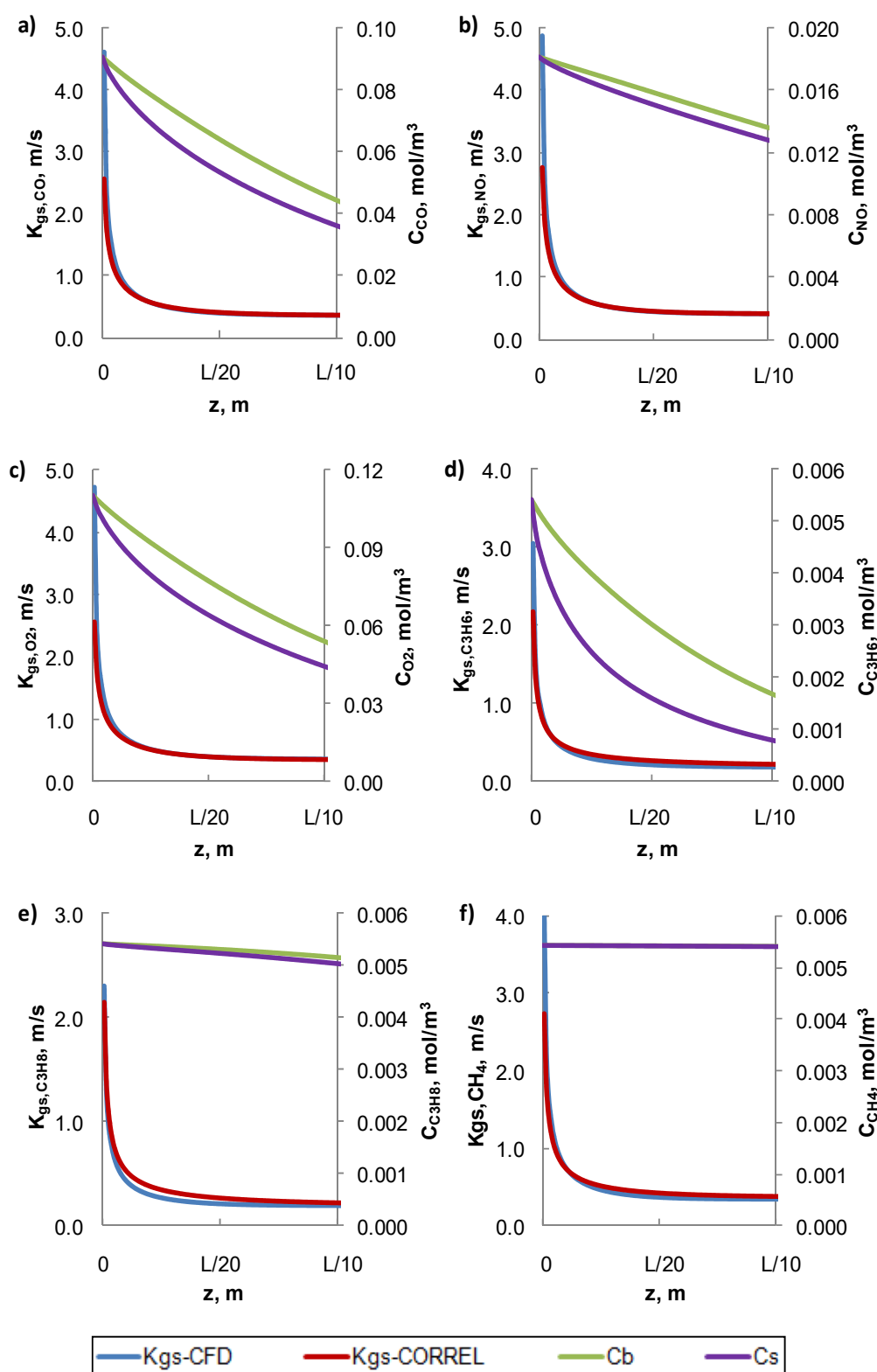


Figure 2. Representative figures for the comparison of K_{gs} profiles along the cell length predicted by the proposed correlation with those derived from CFD calculations as well as a comparison of the concentration profiles in the bulk of the gas phase and over the catalytic surface. Cell diameter $d = 1.1$ mm. Temperature 400 °C. Velocity 0.261 m/s. $Re = 4.6$. (a) CO at lean gas feed composition, (b) NO at rich gas feed composition, (c) O₂ at rich gas feed composition, (d) C₃H₆ at lean gas feed composition, (e) C₃H₈ at rich gas feed composition and (f) CH₄ at rich gas feed composition. Total length $L = 1$ cm.

In Figure 3, the parity plot for the asymptotic values of the $K_{gs,i}$ profiles, i.e., practically for $z > L/10$, for all the species and at all the tested conditions are presented.

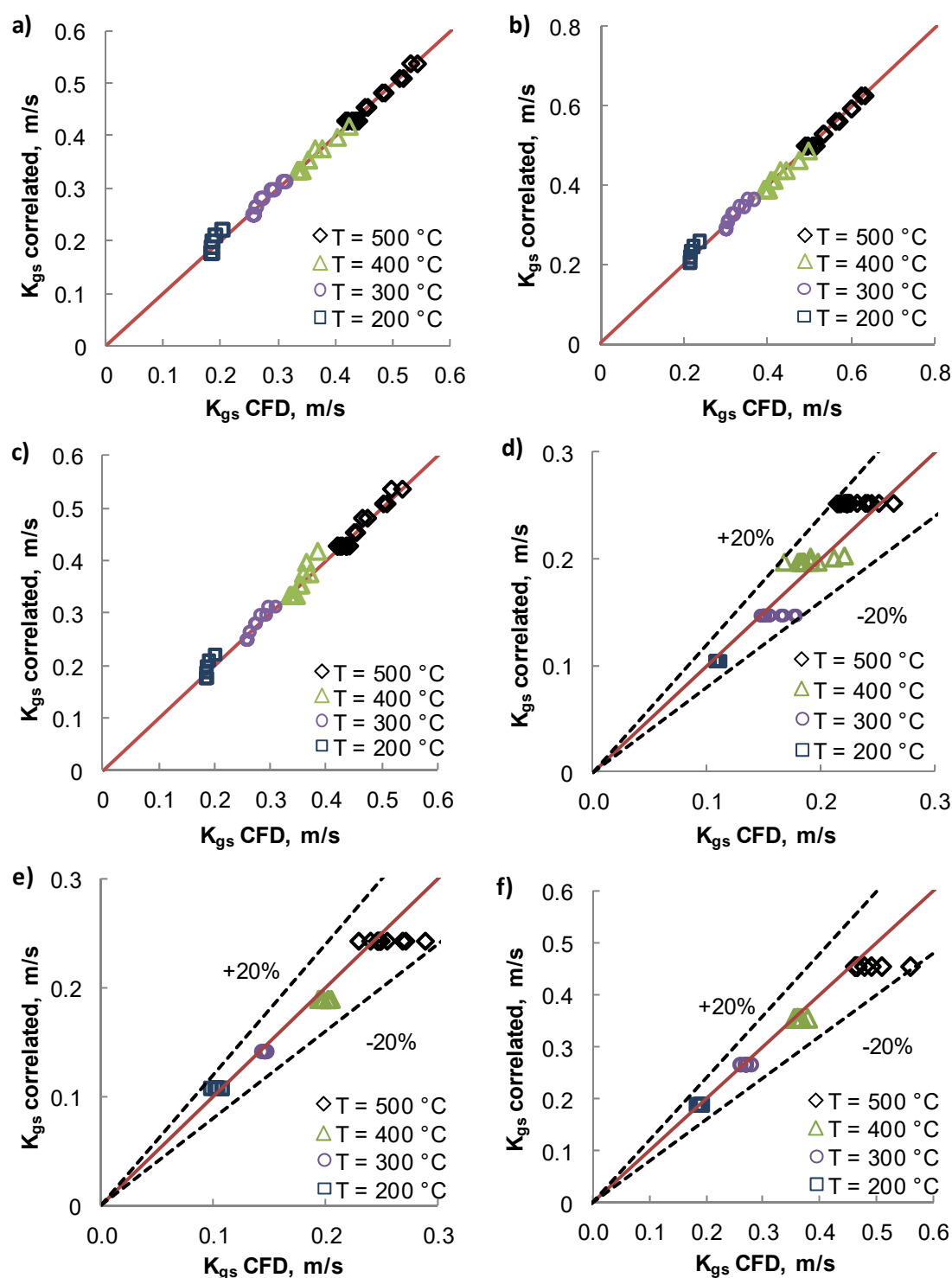


Figure 3. Parity plot for the asymptotic values that the K_{gs} profiles stabilized at all the tested conditions. Cell diameter $d = 1.1$ mm. (a) CO, (b) NO, (c) O₂, (d) C₃H₆, (e) C₃H₈ and (f) CH₄.

For the asymptotic values of the $K_{gs,i}$ profiles a very good fitting was achieved for the species NO, CO and O₂ with a maximum deviation less than 4%. For the species C₃H₆, C₃H₈ and CH₄ a maximum deviation of 20% was achieved between the predicted values and the calculated ones with the detailed CFD model.

The average relative error of prediction of the mass transfer coefficient for CO was 2.1%, for NO 2.3% and for O₂ 2.6% while for CH₄ it was 3.7%, for C₃H₈ 4.2% and for C₃H₆ 7%. These deviations are low and their effects in simulation results were negligible.

The effect of the cell diameter on the mass transfer correlation fitting was tested by conducting CFD calculations with two more cell diameters, 0.9 and 1.3 mm. It was proven that the proposed correlation fit very well to the calculated $K_{gs,i}$ profiles of each species for the two other cell diameters tested. The error of prediction was the same to the one calculated for the cell diameter 1.1 mm for which the correlation was derived.

The effect of the reaction rate on the mass transfer correlation fitting was also tested by conducting calculations with one order of magnitude lower and higher reaction rates for all the reactions taking place. Extreme cases were selected, one order of magnitude lower reaction rates were tested at low temperature 300 °C and one order of magnitude higher reaction rates were tested at high temperature 500 °C. In the case of using one order of magnitude higher reaction rates at 500 °C the average relative prediction error of the correlation was 10.6% for CO, 6.6% for NO, 4.5% for O₂, 10.7% for C₃H₆, 8.6% for C₃H₈ and 5.4% for CH₄. In the case of using one order of magnitude lower reaction rates at 300 °C the average relative prediction error of the correlation was 7.6% for CO, 8.1% for NO, 8.1% for O₂, 8.7% for C₃H₆, 3.3% for C₃H₈ and 2.4% for CH₄.

3.3. 2-D Isothermal CFD Model vs 1-D Isothermal Simplified Model

The effectiveness of a 1-D simplified model that couples PFR with mass transport effects using the correlation for mass transfer of this study was also tested. In Figure 4 a typical diagram of the concentration profiles derived from the 2-D CFD model and the concentration profiles derived from the 1-D model combined with the proposed 1-D correlation for mass transfer are presented for all the species.

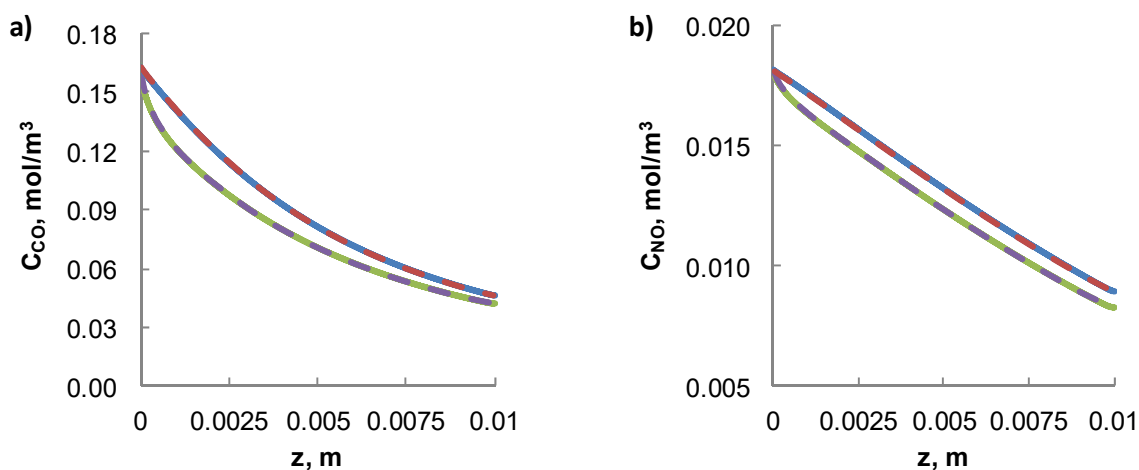


Figure 4. Cont.

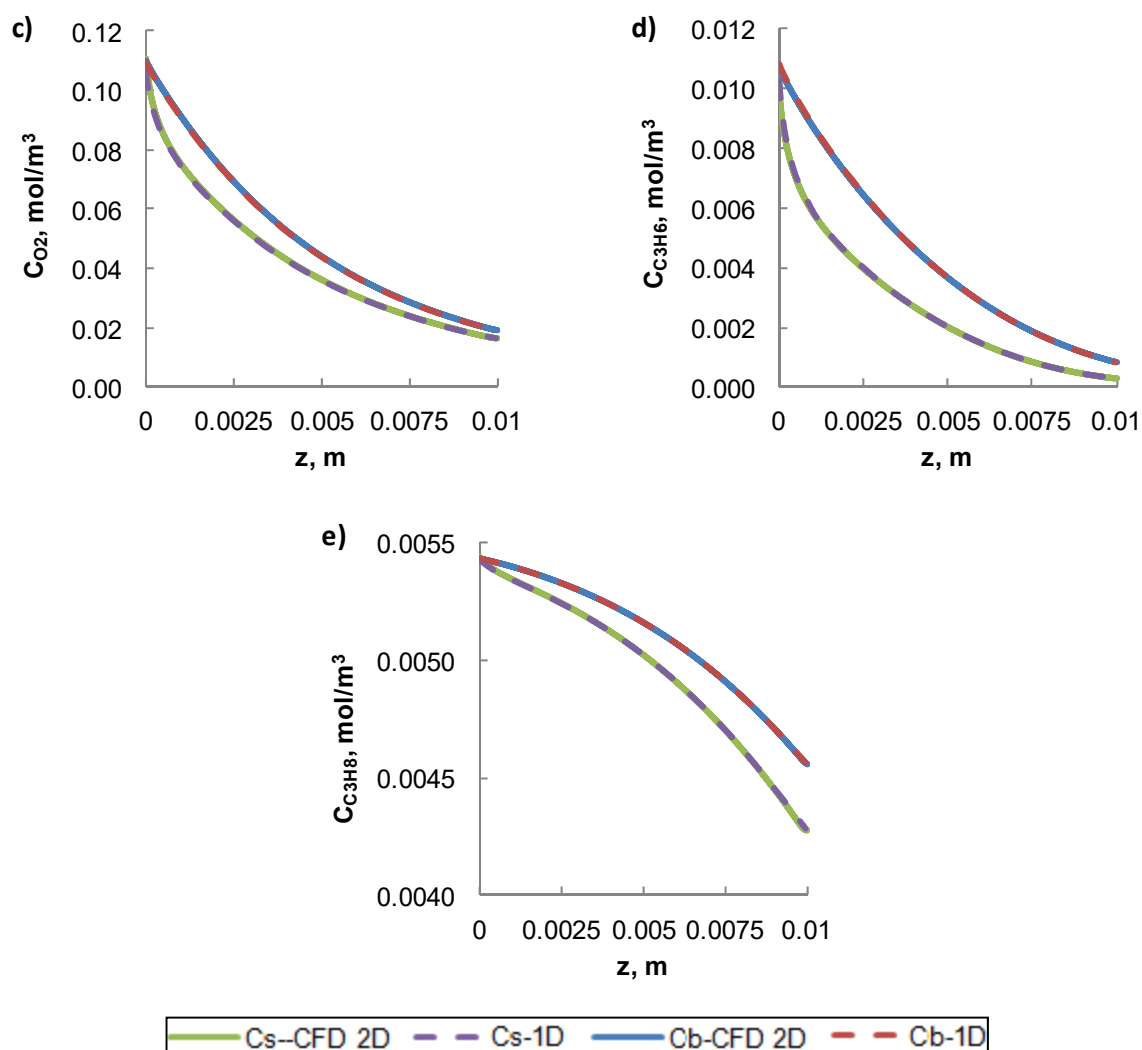


Figure 4. Concentration profiles derived from the 2-D CFD model vs the concentration profiles derived from the 1-D model combined with the 1-D correlation for mass transfer. Rich gas feed composition. Temperature 400 °C. Velocity 1.3 m/s. $Re = 22.7$. (a) CO, (b) NO, (c) O₂, (d) C₃H₆ and (e) C₃H₈.

From the concentration profiles of Figure 4 the operation of monolith was successfully simulated using a 1-D PFR model coupled with gas–solid mass transfer effects as described by the effective mass transfer coefficient derived from the proposed correlation and the predictions are the same like those with the detailed 2-D CFD model.

3.4. Comparison with Other Published Correlations

In Figure 5, a comparison of the mass transfer coefficients in monolith channels predicted by correlations proposed in this work and by Ramanathan et al. [12] and Grigul and Tratz [22] is presented. The correlations proposed by Ramanathan et al. [12] were derived for developing flow and constant wall flux (Sh_F) while those proposed by Grigul and Tratz [22] were derived for fully developed flow and constant wall flux (Sh_F) and constant wall concentration (Sh_T). Typical diagrams of mass transfer coefficient for CO along the cell length at temperature 400 °C are presented for five values of Re in the range of the Re tested.

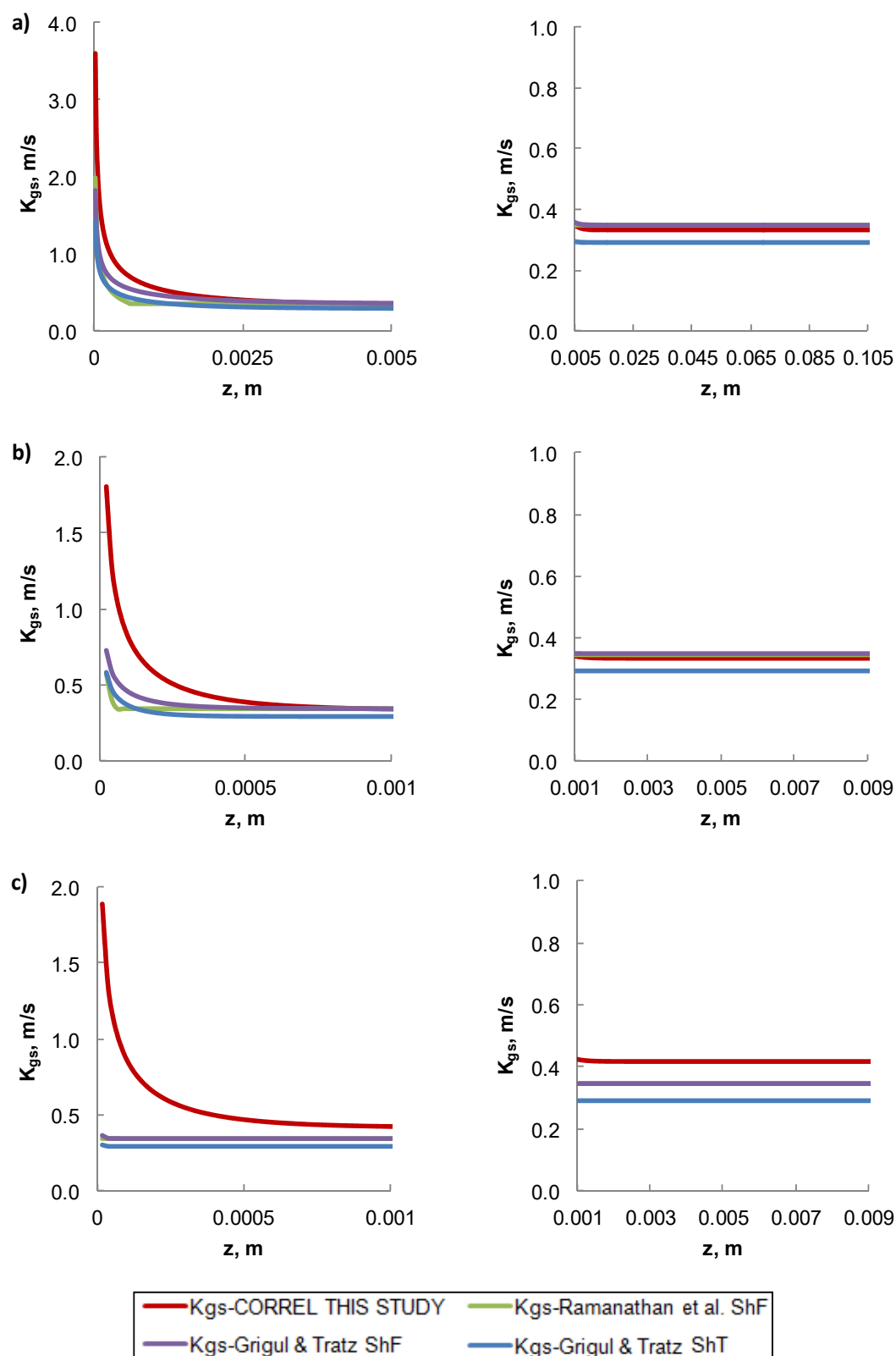


Figure 5. Comparison of the mass transfer correlation for monoliths published in the literature by Ramanathan et al. [12] and Grigul and Tratz [22] with the one proposed in this paper. Diagrams of mass transfer coefficient along the cell length for CO species at temperature 400 °C. Cell diameter $d = 1.1$ mm. (a) Velocity $u = 6.27$ m/s. $Re = 109$, (b) Velocity $u = 0.521$ m/s. $Re = 9$, (c) Velocity $u = 0.033$ m/s. $Re = 0.58$.

The correlations published by Ramanathan et al. [12] and Grigul and Tratz [22] show deviation of the mass transfer coefficient at the initial part that the mass transfer coefficient decreases with the cell length. The error of prediction at this part is getting significantly big especially at low velocities. The correlations published by Ramanathan et al. [12] and Grigul and Tratz [22] for the constant wall flux fit satisfactorily to the asymptotic values that were predicted with the correlation of this study. Some deviations that are not high were observed for the lower velocities.

4. Heat Transfer Coefficients

4.1. Calculation of Effective Heat Transfer Coefficient Profiles Along the Cell

The effective heat transfer coefficient K_t , was calculated running the detailed non-isothermal 2-D CFD model and combining its results with the following 1-D model equation along the channel length:

$$(q)_z = (K_t)_z((T_s)_z - (T_b)_z). \quad (29)$$

For the calculation of the bulk temperature profiles along the cell's length, the mean radial temperature was calculated at each ordinate of the length according to the following equation:

$$(\bar{T}_b)_z = \left(\frac{1}{\pi R^2}\right) \int_{r=0}^{r=R} (T)_{z,r} \cdot 2 \cdot \pi \cdot r \cdot dr. \quad (30)$$

The heat transfer coefficient changes with the coordinate of the length z . A typical profile of heat transfer coefficient along the monolith cell length is presented in Figure 6.

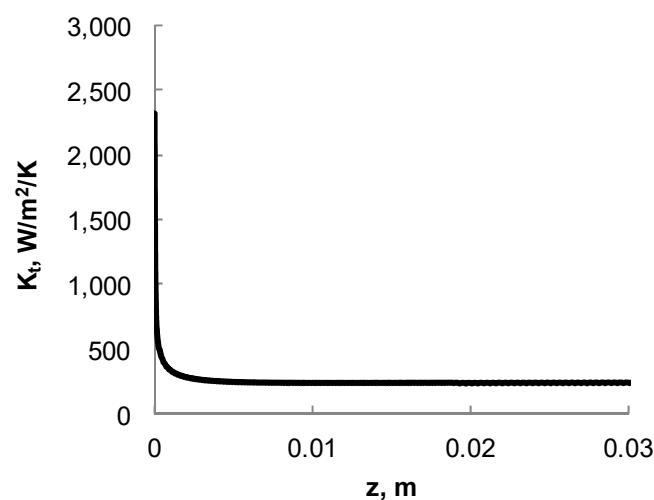


Figure 6. Typical profile of heat transfer coefficient along the monolith cell length.

As shown in Figure 6 the heat transfer coefficient near the entrance has a high value and it steeply decreases at the first mms from the cell entrance, reaching in some cases a plateau or having a small inclination with the length at high velocities.

4.2. Correlation of the Heat Transfer Coefficient K_t

The heat transfer coefficient values along the monolith cell length were correlated with operating conditions by using dimensionless numbers of Nusselt, Prandtl and Reynolds according to the following equation:

$$\text{Nu}(z) = a + b \cdot (z^* \cdot 10^3)^c \exp(e \cdot z^*), \quad (31)$$

where:

$$z^* = \frac{z}{d} \frac{1}{\text{Re} \cdot \text{Pr}}, \quad (32)$$

$$\text{Pr} = \frac{\mu C_p}{k}, \quad (33)$$

$$\text{Nu} = \frac{K_t \cdot d}{k}. \quad (34)$$

The parameter a is related to the K_t value at which the heat transfer coefficient reaches a plateau or alters less significantly with the cell length, away from the cell entrance; the parameter b is related to the initial value that the K_t takes at the cell entrance, and the parameters c and d are related with the curvature of the profile and the distance from the entrance that is demanded for the K_t profile to level off.

The final correlation was derived using eighty (80) profiles of heat transfer coefficient K_t along the cell length at the tested conditions. The Re number at the tested conditions lies within the range 0.51–101.

4.2.1. Heat Transfer Correlation Parameters

For Re lower than 27.5 the Re does not affect the K_t profile and in this case for a better prediction of the proposed correlation, Re must be considered equal to $\text{Re} = 27.5$. Therefore a branched correlation was derived from the fitting of correlation to the K_t profiles that were resulted from CFD calculations.

The best fitting of the correlation to the calculated K_t profiles derived from CFD calculations was achieved for the following parameters.

$$\left. \begin{array}{l} \text{if } u_{\frac{298}{T(K)}} > 0.232 \text{ m/s} \\ \text{if } u_{\frac{298}{T(K)}} < 0.232 \text{ m/s} \\ \text{if } \text{Re} < 27.5 \end{array} \right\} \begin{array}{l} \Rightarrow a = 5.9, b = 23, c = -0.7, d = -40; \\ \Rightarrow a = 5.9 - 0.389 \cdot \ln[u \cdot 298/T] - 0.5857, b = 23, c = -0.7, d = -70; \\ \Rightarrow \text{Re} = 27.5. \end{array}$$

Due to the non-isothermal conditions, the temperature changes along the monolith channel length and thus the gas phase properties such as density, velocity, viscosity, thermal capacity and thermal conductivity must be calculated at each point. For the estimation of the correlation parameters, the alteration of the gas phase properties along the monolith channel was taken into account.

The mean radial property along the channel length was calculated according to the following equation:

$$(\bar{\text{prop}})_z = \left(\frac{1}{\pi R^2} \right) \int_{r=0}^{r=R} (\text{prop})_{z,r} \cdot 2 \cdot \pi \cdot r \cdot dr, \quad (35)$$

where prop is the desirable property to be calculated.

4.2.2. Heat Transfer Correlation Fitting

In Figure 7, typical cases of the correlation fitting to the heat transfer coefficient K_t profile along the monolith cell as derived from CFD calculations are presented at low, middle and high velocities and Re . In these figures the temperature profiles of the bulk of the gas phase and of the gas phase over the catalytic surface are also presented.

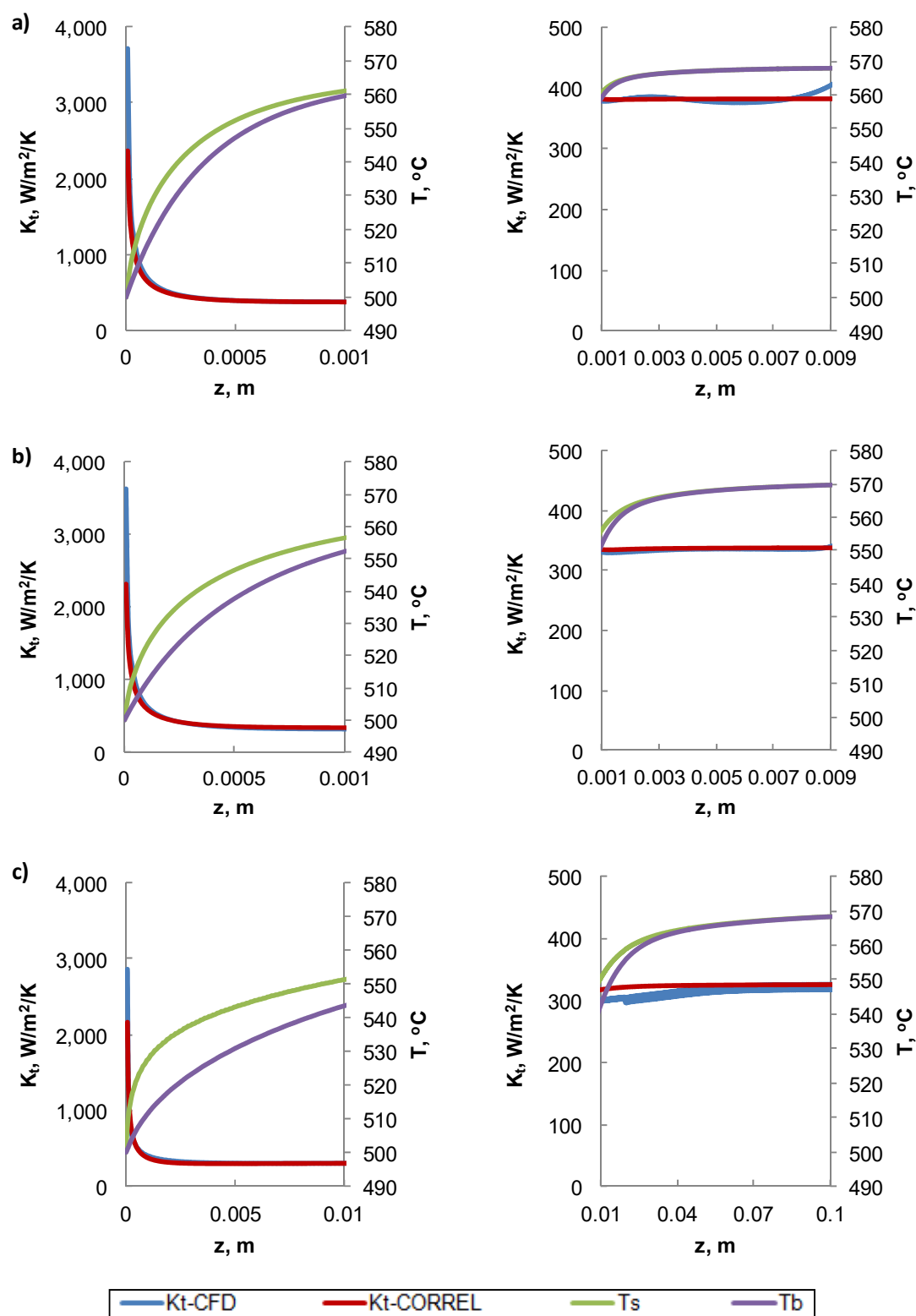


Figure 7. Representative figures for the comparison of K_t profiles along the cell length predicted by the proposed correlation with those derived from CFD calculations as well as comparison of the temperature profile in the bulk of the gas phase and over the catalytic surface. Cell diameter $d = 1.1$ mm. Lean feed composition. Inlet temperature: 500 °C. (a) Inlet velocity 0.037 m/s. $Re = 0.53$, (b) inlet velocity 0.3 m/s. $Re = 4.3$, (c) inlet velocity 7.2 m/s. $Re = 100$.

The average relative error of prediction for the heat transfer coefficients is 2.2%.

The effect of the cell diameter on the heat transfer correlation fitting was tested by conducting calculations with two more cell diameters 0.9 and 1.3 mm. The proposed heat transfer correlation fits very well to the calculated K_f profile for the two other cell diameters tested. The error of prediction is the same to the one calculated for the cell diameter 1.1 mm for which the correlation was derived.

The effect of the reaction rates on the heat transfer correlation fitting was tested by conducting calculations with one order of magnitude lower and higher reaction rates for all the reactions taking place. Extreme cases were selected for the tests, one order of magnitude lower reaction rates at low temperature 300 °C and one order of magnitude higher reaction rates at high temperature 500 °C. In the case of using one order of magnitude higher reaction rates at 500 °C the average relative prediction error of the heat transfer correlation was 3.7%. In the case of using one order of magnitude lower reaction rates at 300 °C the average relative prediction error of the heat transfer correlation was 3.5%.

4.3. Non-Isothermal 2-D CFD Model vs Non-Isothermal 1-D Simplified Model

The effectiveness of the non-isothermal 1-D simplified model that couples PFR with mass and heat transport effects using the correlations for mass and heat transfer of this study was also tested. In Figure 8, a typical diagram of the profiles of the temperature difference between the surface and bulk gas temperature derived from the non-isothermal 2-D CFD model and the profiles derived from the non-isothermal 1-D model combined with the proposed 1-D correlation for mass and heat transfer are presented.

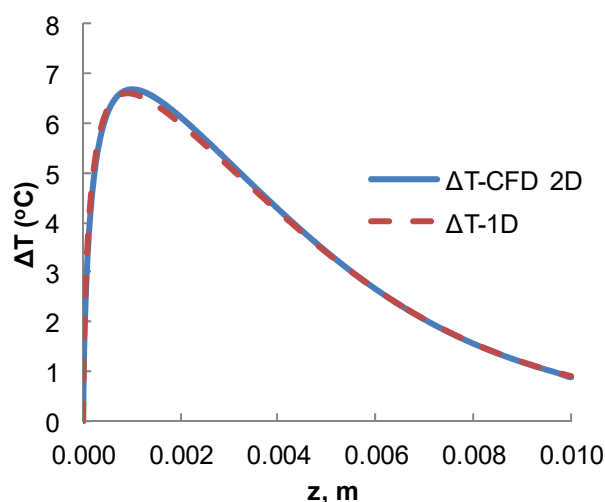


Figure 8. Profiles of the temperature difference between the surface and bulk gas derived from the non-isothermal 2-D CFD model vs the profiles derived from the non-isothermal 1-D model combined with the 1-D correlations for heat and mass transfer. Rich gas feed composition. Inlet temperature 400 °C. Inlet velocity 1.1 m/s. $Re = 19.1$.

From the temperature profiles of Figure 8 it was implied that the operation of monolith was successfully simulated using a 1-D PFR model coupled with mass and heat transfer effects as described by the proposed correlations of this study, and the predictions were practically the same like those with the detailed 2-D CFD model.

4.4. Comparison with Other Published Correlations

In Figure 9, a comparison between the heat transfer coefficient calculated by the proposed correlation in this study and by the correlation proposed by Ramanathan et al. [12] for developing flow and constant wall flux (Nu_F) and by Grigul and Tratz [22] for fully developed flow with constant wall flux (Nu_F) and wall temperature (Nu_T) is presented. Typical diagrams of heat transfer coefficient along the cell length at temperature 400 °C are presented for five values of Re in the range of the Re tested.

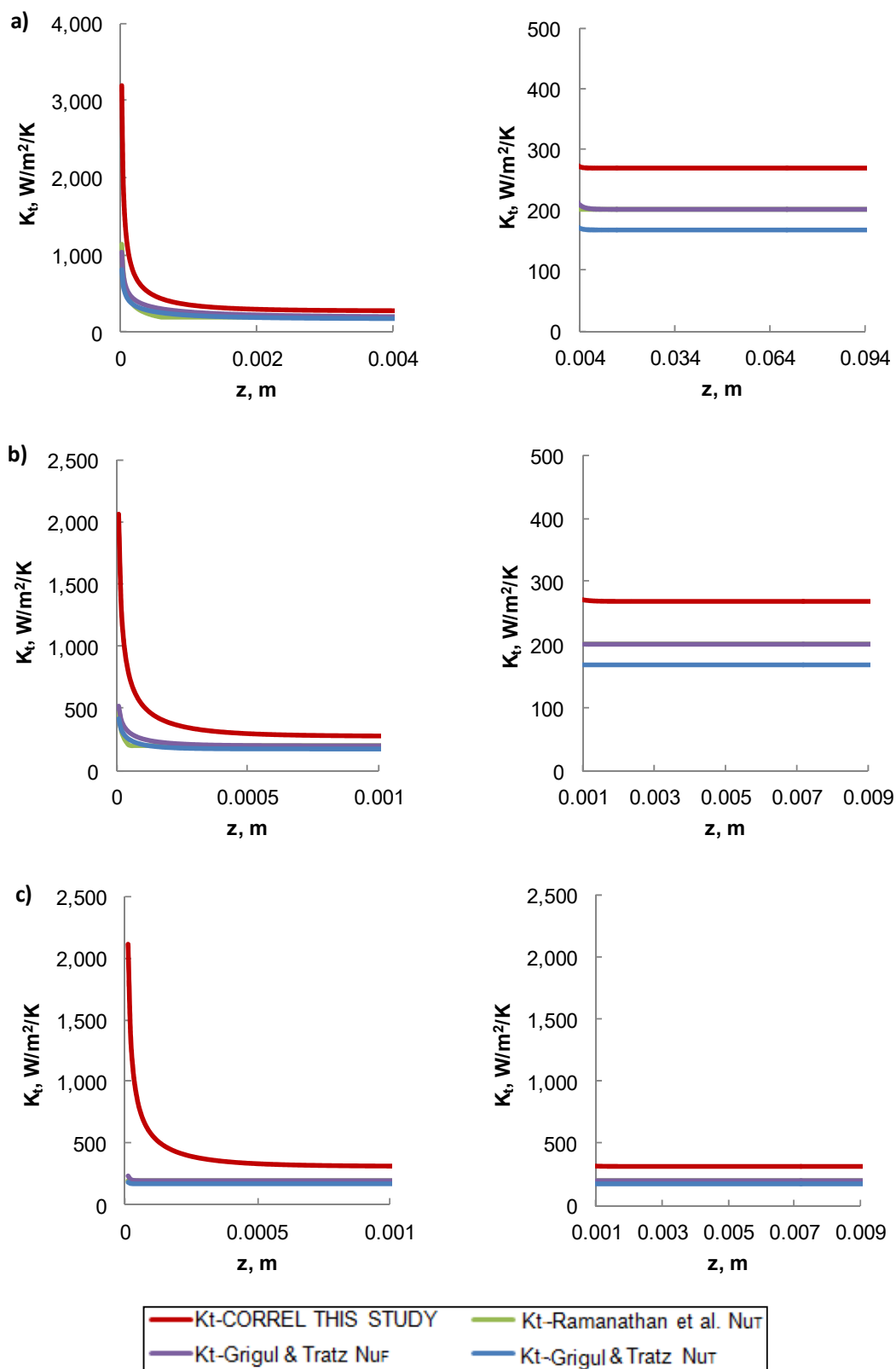


Figure 9. Comparison of the heat transfer correlation for monoliths published in the literature by Ramanathan et al. [12] and Grigul and Tratz [22] with the one proposed in this paper. Diagrams of heat transfer coefficient along the cell length at temperature 400 °C. Cell diameter $d = 1.1$ mm. (a) Velocity $u = 6.27$. $Re = 109$, (b) Velocity $u = 0.521$. $Re = 9$, (c) Velocity $u = 0.033$. $Re = 0.58$.

The heat transfer correlations published by Ramanathan et al. [12] and Grigul and Tratz [22] for the case of the constant wall flux and constant wall temperature show deviations from the prediction of the correlation derived from the CFD calculations in this paper. The differences were very high close to the entrance of the monolith and especially at low gas velocities. The correlation derived from the CFD calculations in this paper shows higher asymptotic values in comparison to the asymptotic values derived from both the constant wall flux Nu_F and constant wall temperature Nu_T correlations of Ramanathan et al. [12] and Grigul and Tratz [22].

5. Conclusions

The mass and heat transfer correlations proposed in this work predicted satisfactorily the mass and heat transfer coefficients profiles along the monolith channel length that were calculated according to thin film theory using the 2-D CFD model within a wide range of velocities and conditions for lab up to real size monoliths.

The fitting of the proposed relations was proven to be very satisfactory for a wide range of reaction rates for all the reactions taking place during operation. The applicability of the correlation was also satisfactory for two other channel diameters 0.9 and 1.3 mm.

Comparing the predictions of the proposed correlations in this study for the mass transfer coefficient with those of other published correlations reveals high deviations at the initial part of the channel where the mass transfer coefficient decreases with the cell length. This is attributed to the fact that the correlations published by Ramanathan et al. [12] were derived for constant wall flux (Sh_F) and by Grigul and Tratz [22] for constant wall flux (Sh_F) and constant wall concentrations (Sh_T). In the case of the constant wall flux, published correlations fitted satisfactorily to the asymptotic K_{gs} values predicted by the correlation of this study. However, those correlations predicted lower K_t values and high deviations from the heat transfer coefficient profiles predicted by the correlation of this study.

A 1-D PFR model coupled with gas–solid mass transfer effects and heat transfer effects by using the proposed mass and heat transfer correlations of this study, successfully simulates the operation of monolith channel, giving the same results with the 2-D CFD model.

Supplementary Materials: The following are available online at <http://www.mdpi.com/2073-4344/9/6/507/s1>, Table S1. Gas feed compositions experimentally tested, Table S2. Set of kinetic parameters of reactions taking place in the simulated monolith. Equations S1.1–S8.2 reactions and reaction rate equations.

Author Contributions: C.C.T.: Methodology software validation, writing—original draft preparation. N.G.P.: conceptualization, methodology, supervision, project administration.

Funding: This research was funded by the European Project No 686086 entitled “Development of novel, high Performance hybrid TWV/GPF Automotive after treatment systems by rational design: substitution of PGMs and Rare earth materials” in the framework of the Horizon 2020 program.

Conflicts of Interest: The authors declare no conflict of interest.

Nomenclature

a, b, c, e	Heat and mass transfer correlation coefficients
C_i	The concentration of component i in the gas phase (mol/m^3)
$C_{i, \text{in}}$	The concentration of component i in the gas phase at cell inlet (mol/m^3)
$C_{i, s}$	The concentration of component i in the gas phase over the catalytic surface (mol/m^3)
$C_{i, b}$	The concentration of component i in the bulk of the gas phase (mol/m^3)
C_p	Thermal capacity of the gas phase (J/K)
d	Diameter of the monolith cell (m)
D_i	The diffusion coefficient of component i in the gas phase (m^2/s)
E_{a_j}	Activation energy of reaction j (J/mol)
\mathbf{I}	Unit vector
K_{ji}	Adsorption constant of component i at reaction j (m^3/mol)
KR_j	Reaction rate constant of reaction j ($\text{m}^4/\text{mol}/\text{s}$)

$K_{gs,i}$	Gas solid mass transfer coefficient for the component i (m/s)
k	Thermal conductivity of the gas phase (W/m/K)
K_t	Heat transfer coefficient (W/m ² /K)
L	Channel length (m)
M_n	Molar mass of the gas phase (Kg/mol)
\mathbf{n}	The vector direction normal to the boundary surface (-)
Nu	Nusselt number (-)
Nu_F	Nusselt number for constant wall flux (-)
Nu_T	Nusselt number constant wall temperature (-)
q	Heat released due to reactions take place on the washcoat wall (W/m ²)
p	Pressure (Pa)
$(\text{prop})_z$	The mean radial property prop at each z ordinate of the length
Pr	Prandtl number (-)
R	Radius of monolith cell (m)
r	Radius coordinate (m)
R_g	Universal constant of gas (= 8.314 J/mol/K)
R_j	Reaction rate of reaction $j = 1, 2, \dots$ (mol/m ² /s)
R_i	Reaction rate of component $i = \text{NO}, \text{CO}, \text{O}_2, \text{C}_3\text{H}_6, \text{C}_3\text{H}_8, \text{CH}_4$ (mol/m ² /s)
Re	Reynolds number (-)
Sh	Sherwood number (-)
Sh_F	Sherwood number for constant wall flux (-)
Sh_T	Sherwood number constant wall concentration (-)
Sc	Schmidt number (-)
S_v	External surface for gas solid mass transfer per void volume (m ² /m ³)
T	Temperature (K)
T_b	Temperature of the bulk of the gas phase (K)
T_s	Temperature of the gas phase over the catalytic surface (K)
\mathbf{u}	The vector of velocity field (m/s)
u	Velocity (m/s)
u_{in}	Velocity at inlet (m/s)
z	Length coordinate, distance from the cell inlet (m)
Greek	
ΔH_R^0	Standard enthalpy of reaction (KJ/mol)
ΔHR_j	Enthalpy of reaction j at temperature T (KJ/mol)
μ	Viscosity (Pas)
ρ	Density of the gas phase (Kg/m ³)

References

- Bertrand, F.; Devals, C.; Vidal, D.; de Prével, C.S.; Hayes, R.E. Towards the simulation of the catalytic monolith converter using discrete channel-scale models. *Catal. Today* **2012**, *188*, 80–86. [[CrossRef](#)]
- Shamim, T. Effect of heat and mass transfer coefficients on the performance of automotive catalytic converters. *Int. J. Engine Res.* **2003**, *4*, 129–141. [[CrossRef](#)]
- Hayes, R.E.; Kolaczkowski, S.T. A study of Nusselt and Sherwood numbers in a monolith reactor. *Catal. Today* **1999**, *47*, 295–303. [[CrossRef](#)]
- Koltsakis, G.C.; Stamatelos, A.M. Catalytic automotive exhaust aftertreatment. *Prog. Energy Combust. Sci.* **1997**, *23*, 1–39. [[CrossRef](#)]
- Iwaniszyn, M.; Piatek, M.; Gancarczyk, A.; Jodłowski, P.J.; Łojewska, J.; Kołodziej, A. Flow resistance and heat transfer in short channels of metallic monoliths: Experiments versus CFD. *Int. J. Heat Mass Transf.* **2017**, *109*, 778–785. [[CrossRef](#)]
- Santos, H.; Costa, M. Analysis of the mass transfer controlled regime in automotive catalytic converters. *Int. J. Heat Mass Transf.* **2008**, *51*, 41–51. [[CrossRef](#)]
- Bhattacharya, M.; Harold, M.P.; Balakotaiah, V. Mass-Transfer Coefficients in Washcoated Monoliths. *AIChE J.* **2004**, *50*, 2939–2955. [[CrossRef](#)]

8. Holmgren, A.; Andersson, B. Mass transfer in monolith catalysts-CO oxidation experiments and simulations. *Chem. Eng. Sci.* **1998**, *53*, 2285–2298. [[CrossRef](#)]
9. Balakotaiah, V.; Gupta, N.; West, D. A simplified model for analyzing catalytic reactions in short monoliths. *Chem. Eng. Sci.* **2000**, *55*, 5367–5383. [[CrossRef](#)]
10. Canu, P.; Vecchi, S. CFD Simulation of Reactive Flows: Catalytic Combustion in a Monolith. *AIChE J.* **2002**, *48*, 2921–2935. [[CrossRef](#)]
11. Arrighetti, C.; Cordiner, S.; Mulone, V. Heat and Mass Transfer Evaluation in the Channels of an Automotive Catalytic Converter by Detailed Fluid-Dynamic and Chemical Simulation. *J. Heat Transf.* **2007**, *129*, 536–547. [[CrossRef](#)]
12. Ramanathan, K.; Balakotaiah, V.; West, D.H. Light-off criterion and transient analysis of catalytic monoliths. *Chem. Eng. Sci.* **2003**, *58*, 1381–1405. [[CrossRef](#)]
13. Depcik, C.; Assanis, D. One-dimensional automotive catalyst modelling. *Prog. Energy Combust. Sci.* **2005**, *31*, 308–369. [[CrossRef](#)]
14. Holder, R.; Bollig, M.; Anderson, D.R.; Hochmuth, J.K. A discussion on transport phenomena and three-way kinetics of monolithic converters. *Chem. Eng. Sci.* **2006**, *61*, 8010–8027. [[CrossRef](#)]
15. Gupta, N.; Balakotaiah, V. Heat and mass transfer coefficients in catalytic monoliths. *Chem. Eng. Sci.* **2001**, *56*, 4771–4786. [[CrossRef](#)]
16. Hayes, R.E.; Kolaczowski, S.T. Mass and heat transfer effects in catalytic monolith reactors. *Chem. Eng. Sci.* **1994**, *49*, 3587–3599. [[CrossRef](#)]
17. Hawthorn, R.D. Afterburner catalysts-effects of heat and mass transfer between gas and catalyst surface. *Am. Inst. Chem. Eng.* **1974**, *21*, 849–853.
18. Votruba, J.; Mikus, O.; Nguen, K.; Hlavacek, V.; Skrivanek, J. Heat and mass transfer in monolithic honeycomb catalysts—II. *Chem. Eng. Sci.* **1975**, *30*, 201–206. [[CrossRef](#)]
19. Bennett, C.J.; Kolaczowski, S.T.; Thomas, W.J. Determination of heterogeneous reaction kinetics and reaction rates under mass transfer controlled conditions for a monolith reactor. *Trans. Inst. Chem. Eng. Part B* **1991**, *69*, 209–220.
20. Ullah, U.; Waldram, S.P.; Bennett, C.J.; Truex, T. Monolithic reactors: Mass transfer measurements under reacting conditions. *Chem. Eng. Sci.* **1992**, *47*, 2413–2418. [[CrossRef](#)]
21. Uberoi, M.; Pereira, C.J. Mass transfer coefficients for monolith catalysts. *Ind. Eng. Chem. Res.* **1996**, *35*, 113–116. [[CrossRef](#)]
22. Grigull, U.; Tratz, H. Thermischer Einlauf in ausgebildeter laminarer Rohrströmung. *Int. J. Heat Mass Transf.* **1965**, *8*, 669–678. [[CrossRef](#)]
23. Shah, R.K.; London, A.L. *Laminar Flow Forced Convection in Ducts*; Academic Press: New York, NY, USA, 1978.
24. Tronconi, E.; Forzatti, P. Adequacy of lumped parameter models for SCR reactors with monolith structures. *AIChE J.* **1992**, *38*, 201–210. [[CrossRef](#)]
25. Kirchner, T.; Eigenberger, G. Optimization of the cold-start behavior of automotive catalysts using an electrically heated pre-catalyst. *Chem. Eng. Sci.* **1996**, *51*, 2409–2418. [[CrossRef](#)]
26. Gundlapally, S.R.; Balakotaiah, V. Heat and mass transfer correlations and bifurcation analysis of catalytic monoliths with developing flows. *Chem. Eng. Sci.* **2011**, *66*, 1879–1892. [[CrossRef](#)]
27. Groppi, G.; Belloli, A.; Tronconi, E.; Forzatti, P. A comparison of lumped and distributed models of monolith catalytic reactors. *Chem. Eng. Sci.* **1995**, *50*, 2705–2715. [[CrossRef](#)]
28. Heck, R.H.; Wei, J.; Katzer, J.R. Mathematical modelling of monolithic catalysts. *AIChE J.* **1976**, *22*, 477–483. [[CrossRef](#)]

